JTTEE5 13:405-414
DOI: 10.1361/10599630419328
1059-9630/$19.00 © ASM International

Bending Behavior of HVOF Produced WC-17Co Coating: Investigated by Acoustic Emission

S. Bouaricha, J-G. Legoux, and P. Marcoux

(Submitted March 12, 2003; in revised form May 29, 2003)

A four-point bend test using acoustic emission (AE) was used to compare coating properties under mechanical solicitation, mainly the toughness and spalling behavior. Coatings are made from the same material; Sulzer-Metco (Westbury, NY) 2005NS (WC-17Co) sprayed with an HVOF gun with different spray parameters. Coatings deposited on thin rectangular substrates were first bent in tension then in compression. AE features like the event number, energy per event, and cumulative energy were used to assess the damages in the coatings. The results are analyzed in relation to the coating microstructure.

Keywords acoustic emission, cermet coatings, four-point bending test, HVOF, thermal spray, WC-Co

1. Introduction

WC-Co-Cr and WC-Co coatings are largely used for wear resistance applications. Their behavior under tests like erosion, abrasion, and corrosion has been studied in numerous publications. However, unlike thermal barrier coatings (TBCs),[1-6] there are few studies dedicated to the evaluation of WC-based materials under mechanical solicitations such as the bend test coupled with acoustic emission.[7-9]

This test could be a mean of predicting deleterious failure phenomenon like coating spalling or delamination from the substrate. It allows establishing a better understanding of the relationship among processing, microstructure, and coating properties.

The test consists of a four-point bending test, which allows the online monitoring of the damage development of the coatings. Indeed, it is performed by simultaneously applying a certain strain rate, while measuring and analyzing the characteristics of acoustic emissions. The formation of a crack during loading releases energy in the form of an acoustic wave, which propagates through the sample and may be detected using a piezoelectric sensor attached to the sample. Generally, cracks are known to either nucleate from defects, which are located within and between adjacent splats or are already present in the coatings prior to the bending test.

In four-point bend evaluation, the acoustic emissions (AEs) are known as burst type events. Analyzing their features allows a comparison among different samples that exhibit specific mechanical behaviors due to their different microstructures.

In this study, an attempt will be made to correlate the coating damage after bending and the characteristics of the acoustic emissions recorded during the mechanical solicitation.

S. Bouaricha, J-G. Legoux, and **P. Marcoux,** National Research Council Canada, 75 de Mortagne, Boucherville J4B 6Y4, Québec, Canada. Contact e-mail: Salim.Bouaricha@imi.cnrc-nrc.gc.ca.

2. Experimental Details and Set-Up

2.1 In-Flight Particles and Coatings Characterization

The diagnostic system DPV-2000 (Tecnar Automation, St.-Bruno, Québec, Canada) was used to measure the in-flight temperature, velocity and mean particle size during spraying.

Microhardness ($HV_{0.3}$) was averaged from ten random indentations on the cross section of the coatings, with a load of 300 g and duration of 20 s.

The initial powder and coatings were examined using a Hitachi S-4700 (Rexdale, Ontario, Canada) scanning electron microscope (SEM). The polished longitudinal side planes between inner spans of the four-point bend test were observed. Before SEM observations, all deformed coatings were entirely vacuum impregnated in epoxy resin to stabilize cracks generated by the bend test and cut in two places at the positions where the inner spans of the four-point bend test were placed. The coatings were vacuum impregnated in epoxy resin a second time before finally been polished. These steps insure to avoid creating new cracks during cutting and polishing procedures.

X-ray diffraction (XRD) measurements were carried out using a Bruker-AXS (Madison, WI) diffractometer with Cu K_α radiation to determine the phases present in the coatings.

Residual stresses were evaluated from the curvatures of an Almen strip type N.

2.2 Thermal Spraying

The starting feedstock material is the D-2005NS spray-dried and sintered powder from Sulzer-Metco (Westbury, NY), made of 83WC and 17Co in weight percentage as assessed by the manufacturer.

Coatings made from this powder were sprayed using the Diamond Jet HVOF gun (Sulzer Metco), with hydrogen as fuel and

Table 1 Sets of Spray Parameters Used for the Diamond Jet HVOF Gun to Produce Samples #1 to #8

Parameter Sample ID	1 Ratio H_2/O_2	2 Total Gas (l/min)	3 SOD (cm)	4 Carrier Gas N_2, l/min	5 Substrate Surface *T*, °C	6 Thickness/ Pass, μm	Coating's Thickness, mm	Feed Rate, g/min	H_2, l/min	O_2, l/min	Air, l/min
#1	2.4	1220	22.9	17.5	175	2.5	0.94	38	600	250	350
#2	2.4	1220	22.9	24	225	10.2	1.07	38	600	250	350
#3	2.4	1320	29.2	17.5	175	10.2	0.97	38	655	275	375
#4	2.4	1320	29.2	24	225	2.5	0.98	38	655	275	375
#5	3.6	1220	29.2	17.5	225	2.5	1.01	38	680	190	340
#6	3.6	1220	29.2	24	175	10.2	0.93	38	680	190	340
#7	3.6	1320	22.9	17.5	225	10.2	1.02	38	720	200	380
#8	3.6	1320	22.9	24	175	2.5	0.98	38	720	200	380

different sets of spray parameters. They were deposited onto grit-blasted mild steel substrates. Substrates have rectangular shape (Almen strip type N) with a size of 79.2 mm in length, 19.2 mm in width and approximately 1 mm in thickness.

Spray parameter sets are listed in Table 1. They were defined to produce different coatings for further evaluation. An L-8 orthogonal array was used to produce coatings with eight sets of spray conditions. The spray parameters and their effects were analyzed using standard procedures for a Taguchi type matrix, based on design of experiments (DOE) to find quantitative relationships, as those described in a previous paper.[10] The following parameters were chosen as independent variables: H_2/O_2 ratio, total gas flow, spraying stand-off distance, carrier gas flow, substrate temperature, and thickness per pass. Each parameter varied between two levels.

A total of four samples were produced for each spray parameter set. A special cylindrical shape sample-holder was designed to contain the four samples. During thermal spraying, the cylinder rotated around its longitudinal axis, insuring that all the samples would be produced with similar thickness and substrate temperature. The temperature of the substrate was monitored using a pyrometer. An air jet directed onto the surface of the samples was used for cooling to maintain the average temperature of the substrates at the desired value.

2.3 Four-Point Bending Test

The four-point bending test set up was designed in our laboratory. The lengths of the inner and outer spans were 20 and 50 mm, respectively. The motion of stress points is driven by a stepping motor power driver (from Klinger Scientific Corp., Garden City, NY), which allows a continuous crosshead displacement rate as low as 50 μm/s.

2.4 Acoustic Emission

The AE signals were detected by a piezoelectric sensor having a diameter of 6 mm (Panametrics, Montreal, Québec) and a frequency response up to 1.5 MHz. The sensor signal was captured by an acquisition board card NI 5112 from National Instrument (Austin, TX). Data acquisition was processed using a diagnostic apparatus developed in our laboratory and the post-test analysis was performed using a program built from LabView software (National Instrument).

Typically, an input AE signal that crosses a preset threshold level acts as a trigger signal. During testing, the acquired signals were preamplified and stored on the computer for subsequent data processing. Adequate filtering and threshold settings eliminated noises, created by the testing machine at known frequency and the specimen grips, which is a continuous type signal. Ultrasonic grease was used as a couplant between the sensor and the coupon. The capture rate was set so that the time length saved for each digitized waveform was 2 ms, including a 0.2 ms pretrigger before the waveform, to delineate the beginning of the waveform. The measurements of AE signals were representative after testing two to four samples.

3. Results and Discussion

3.1 Bending Test

Only tensile bending tests were performed on all coatings. However, compressive bending tests were also performed on the coatings but did not give reliable AE signatures. Indeed, for all coatings bent in compression, the few recorded AE events were of weak AE energy and a close look to their signal shapes shows that they are likely formed from Almen sliding in between the four point of the bend test rather than real AE generated by cracks.

The 20 mm central region of the sample was in pure bending (constant bending moment and no shear forces). Thus, the bend test was run until a maximum deflection of 5 mm was achieved and a crosshead speed of 50 μm/s. This maximum deflection corresponds by calculation (Appendix 1) to about 0.91% strain for 1 mm thick sample in the tensile surface of the substrate. The value of 5 mm in deflection was chosen in such way that after loading the substrate alone (Almen strip without coating), no permanent bending remains on it.

Figure 1 shows strain as a function of the deflection for the four-point bend test; $\varepsilon 1$ and $\varepsilon 2$ represent the strains for the metallic substrate without coating, whereas $\varepsilon 3$ and $\varepsilon 4$ are the strains for the substrate with coating #6, which was randomly chosen. Strains $\varepsilon 1$ and $\varepsilon 3$ were measured from strain gauge while applying deflection during the four-point bend test, while strains $\varepsilon 2$ and $\varepsilon 4$ were derived from the formula that takes into account the applied deflection, the thickness of the tested sample, and the distances (inner and outer spans) between loading and support bars of the four-point bend test. In the case where only the metallic substrate was deformed, it demonstrates that values of strain from the formula exhibit a good fitting with those measured by the strain gauge. On the other hand, the strain for the coating-substrate sample is slightly different but stays within a

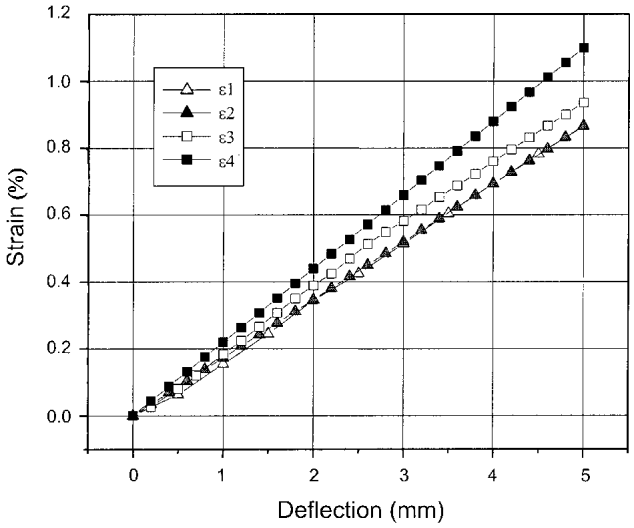

Fig. 1 Strain as a function of the deflection with the four-point bend test, $\varepsilon 1$ and $\varepsilon 2$ for substrate without coating, and $\varepsilon 3$ and $\varepsilon 4$ with coating (#6, randomly chosen); $\varepsilon 1$ strain for substrate (Almen-type N) measured from strain gauge, $\varepsilon 2$ strain for substrate (Almen-type N) calculated with the measured deflection, $\varepsilon 3$ strain for coating on substrate (Almen-type N) measured from strain gauge, $\varepsilon 4$ strain for coating on substrate (Almen-type N) calculated with the measured deflection

range of 10% of error. Indeed, the difference between calculated ($\varepsilon 4$) and measured ($\varepsilon 3$) strains has proportionally increased with the applied deflection. A few explanations can be provided to substantiate this imperfect fitting. First, the deflection equation is most probably limited to the cases where the thickness of the coating is much smaller than the thickness of the substrate. The experiments presented here attempted to respect that limit by using coating thickness below 10% of the substrate's thickness. Second, mostly due to their different modulus of elasticity, coatings behave differently from their monolithic substrate. Finally, as will be shown later on, the apparition of cracks in the coating, which releases stress, changes the cross section and the stiffness of the coating/substrate system, which has a direct impact on the deflection of the sample.

3.2 Effect of Parameters on Particles Temperature and Velocity

The average particle temperature and velocity profiles were calculated from the four profiles obtained with a parameter set at one level and were compared with the average profile for the same parameter set at its second level, as explained in Sec. 2.2.

From Fig. 2, the effects of H_2/O_2 ratio, total gas and carrier gas parameters on in-flight temperature and velocity of the particles can be summarized as follows:

- At all stand-off distance, the increase in the stoichiometry (H_2/O_2 ratio) from 2.4-3.6 increases the in-flight temperature but slightly decreases the velocity.
- Increasing the total gas from 1220 to 1320 l/min., increases both temperature and velocity.
- The carrier gas has no effect on temperature and velocity when varied from 17.5 to 24 l/min.

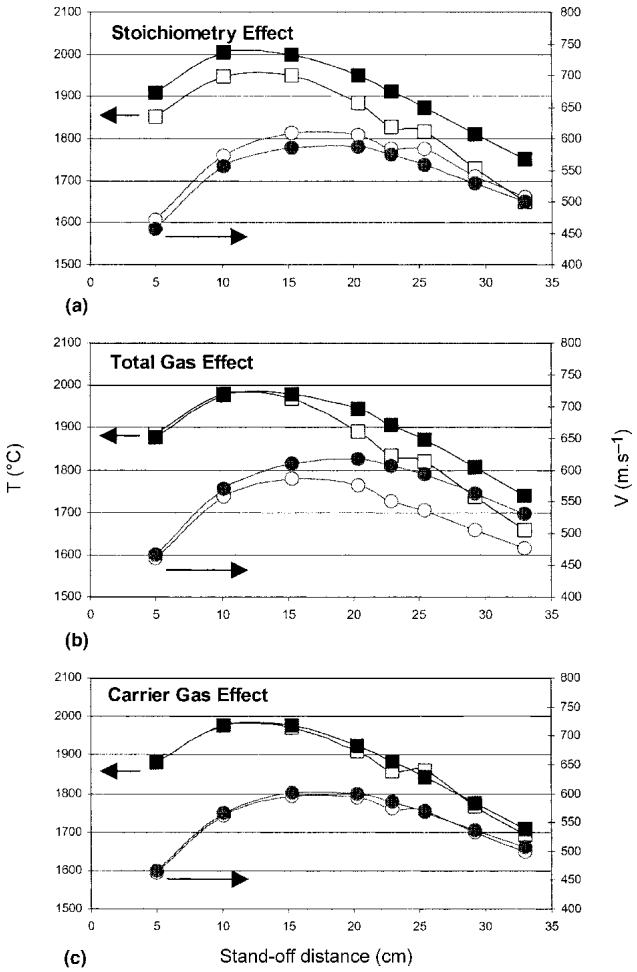

Fig. 2 Effect of spraying parameters on in-flight particles temperature and velocity (square marks for temperature and circle marks for velocity, open and full marks for lowest and highest levels, respectively, of the studied parameter as presented in Table 1

Table 2 In-Flight Particles Temperature and Velocity; Coatings Microhardness and Compressive Residual Stresses (Stress is Normalized for Similar Thickness)

Sample ID	*V*, m/s	*T*, °C	H_v (St. Dev.), kgf/mm^2	Almen, mm(a)
#1	538	1746	1082.7 (80.6)	0.0111
#2	568	1804	1200.3 (109.1)	0.0421
#3	566	1754	1120.2 (72.3)	0.0099
#4	571	1794	1091.3 (73.9)	0.0112
#5	498	1795	1111.2 (70.3)	0.0077
#6	505	1775	1057.2 (68.3)	0.0055
#7	599	1923	1202.4 (91.2)	0.0128
#8	600	1943	1121.1 (97.2)	0.0096

(a) From curvature of the Almen strip in compression

Table 2 shows the in-flight particles temperature and velocity, of particles for coatings #1 to #8 at stand-off distances, as defined earlier in Table 1. It also indicates the microhardness and the residual stresses obtained from curvature of Almen strips. Due to the different coating thicknesses, curvatures were normalized to an Almen thickness value of 1 mm.

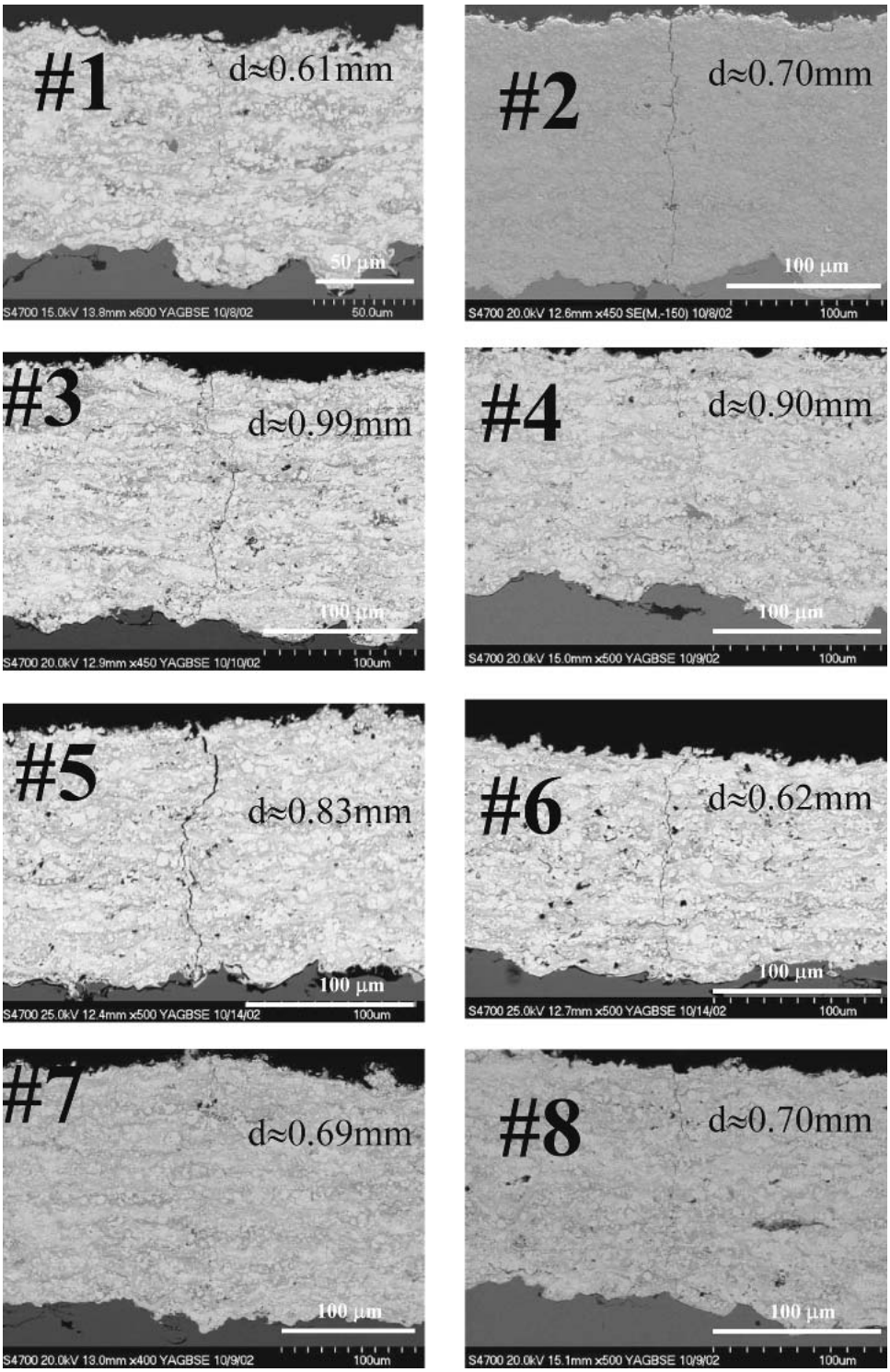

Fig. 3 Cracks images for deformed coatings #1 to #8 obtained by SEM; *d* is the average distance separating the transversal cracks

3.3 Microstructure Characterization

First of all, it is important to mention that all produced coatings presented a very low porosity, typically less than 1%, as determined by image analysis. Figure 3 shows SEM microstructures for coatings #1 to #8 after the four-point bend test. The density and morphology of the cracks qualitatively represent the major damages in the observed area.

None of the studied coatings spalled out or delaminated from their substrates. All coatings exhibited clearly defined transversal cracks. The cracks apparently propagated from the surface, normal to the load axis, to the coating-substrate interface with-

out branches, and then propagated parallel along the interface. Surface defects and defects within the coating lead to stress concentrations and are believed to constitute the cracking origins and paths, respectively. Also, it can be noted in all coatings that cracks were observed to be regularly spaced with distances varying from 0.4 to 1.1 mm (not shown here). The average distance *d* separating two cracks is reported in Fig. 3. Cracks formed in the coatings at regular intervals are consistent with the four-point bend test since the cracks will relieve the stress in a uniform manner. Depending on spray conditions, similar observations were already mentioned in numerous publications.[6,9,11]

The averaged width (opening) of transversal and interfacial cracks was determined qualitatively from image analysis of four cracks. It also was found to vary with coatings. Indeed, coating #5 (~1.5-2.0 μm) has the largest cracks, followed by #6 (~0.8-1.0 μm), while coatings #1 (~0.5-0.7 μm) and #7 (~ 0.3-0.5 μm) exhibit the smallest crack opening.

The XRD patterns for coatings #1 to #8 were examined. They revealed that all coatings consist of WC as the major phase, with W_2C and W in small amounts resulting from the WC decarburization. No clear peak related to the Co phase was found. On the other hand, all patterns show a broad diffraction halo at a range of 2θ ~ (37°, 47°). This indicates the presence of a quantity of an amorphous or nanocrystalline phase in each coating, probably composed of W, Co and C. Figure 4 shows an example of the XRD patterns for coatings #2 and #3.

For all coatings, peaks related to W_2C and W phases are very small, which makes for instance, their quantification difficult by the Rietveld method. However, it is possible by using other means, to compare the amorphous fraction present in coatings.

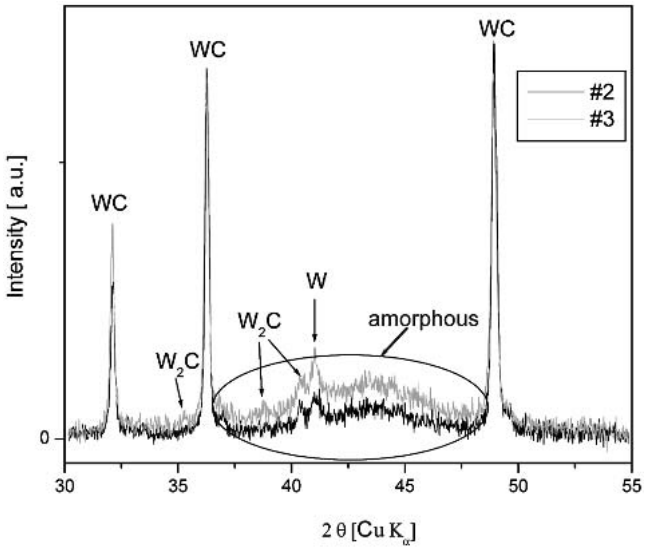

Fig. 4 X-ray diffraction patterns of coatings #2 and #3

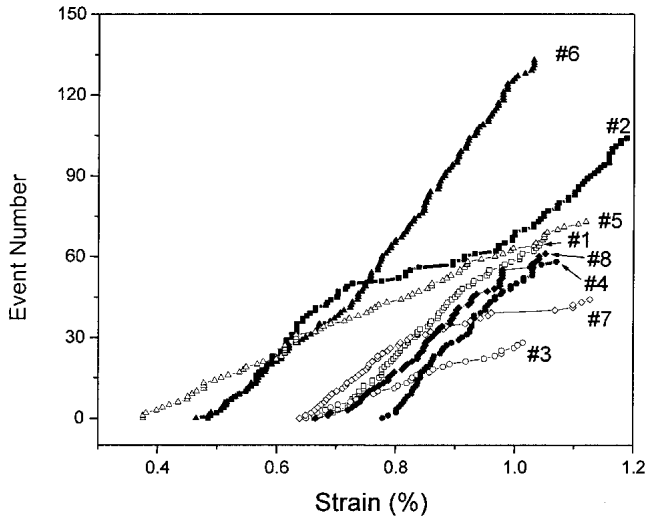

Fig. 5 AE event number versus strain

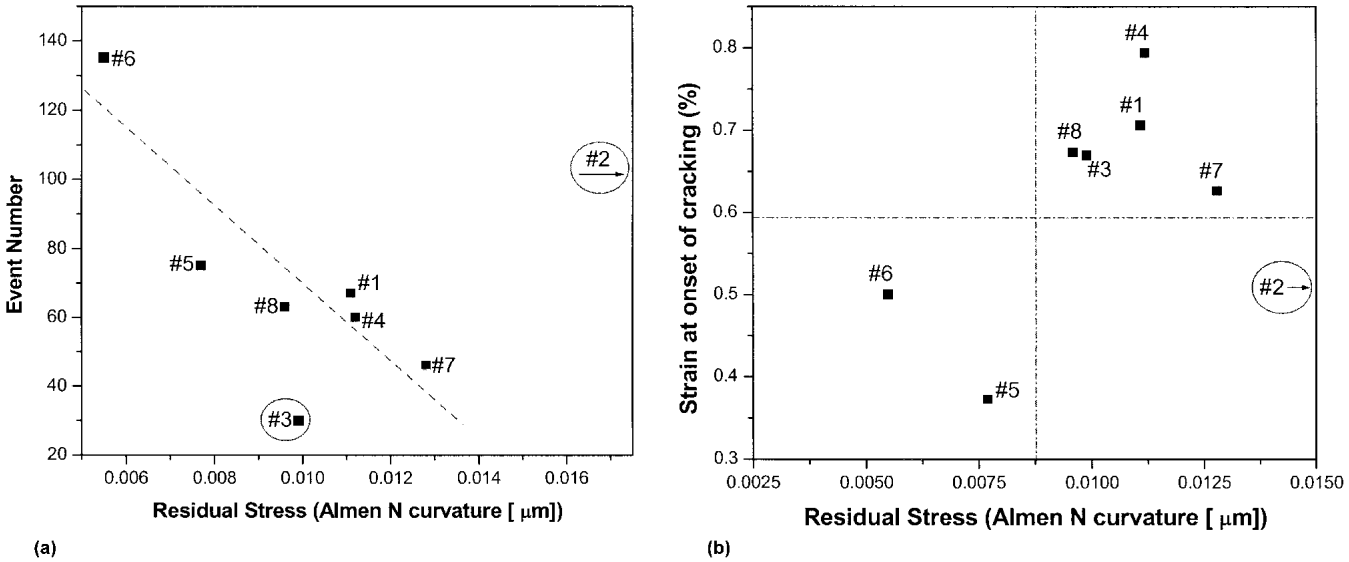

Fig. 6 Residual stresses obtained from Almen curvature versus **(a)** AE event number and **(b)** onset of cracking

This is possible by using the index of crystallinity (I_c) as adopted by Verdon et al.[12] The I_c is defined as the ratio between the areas of the Bragg peaks (crystalline material) and the total areas of the spectrum for 2θ between 30° and 55°. It gives relative proportions of crystalline and amorphous materials. Since one does not have the amorphous structure factor, the values obtained for I_c are not absolute but can be used to rank the materials in a relative manner. Thus, the larger I_c is, the more the coating is composed of crystalline material and undergone less carbide degradation. Table 3 shows the crystallinity index for all coatings. For example, it can be seen that coating #2 is less degraded than coating #3 (shown in Fig. 4), which is reflected by a higher portion of crystalline WC phase and I_c value.

Table 3 Indexes of Crystallinity for Coatings #1 to #8

Sample ID	I_c
#1	0.597
#2	0.613
#3	0.445
#4	0.489
#5	0.475
#6	0.573
#7	0.530
#8	0.567

3.4 Acoustic Emission Features

Figure 5 shows the number of events in function of strain recorded for the bent coatings #1 to #8. The total number of events from the tests could distinguish the AE feature of either

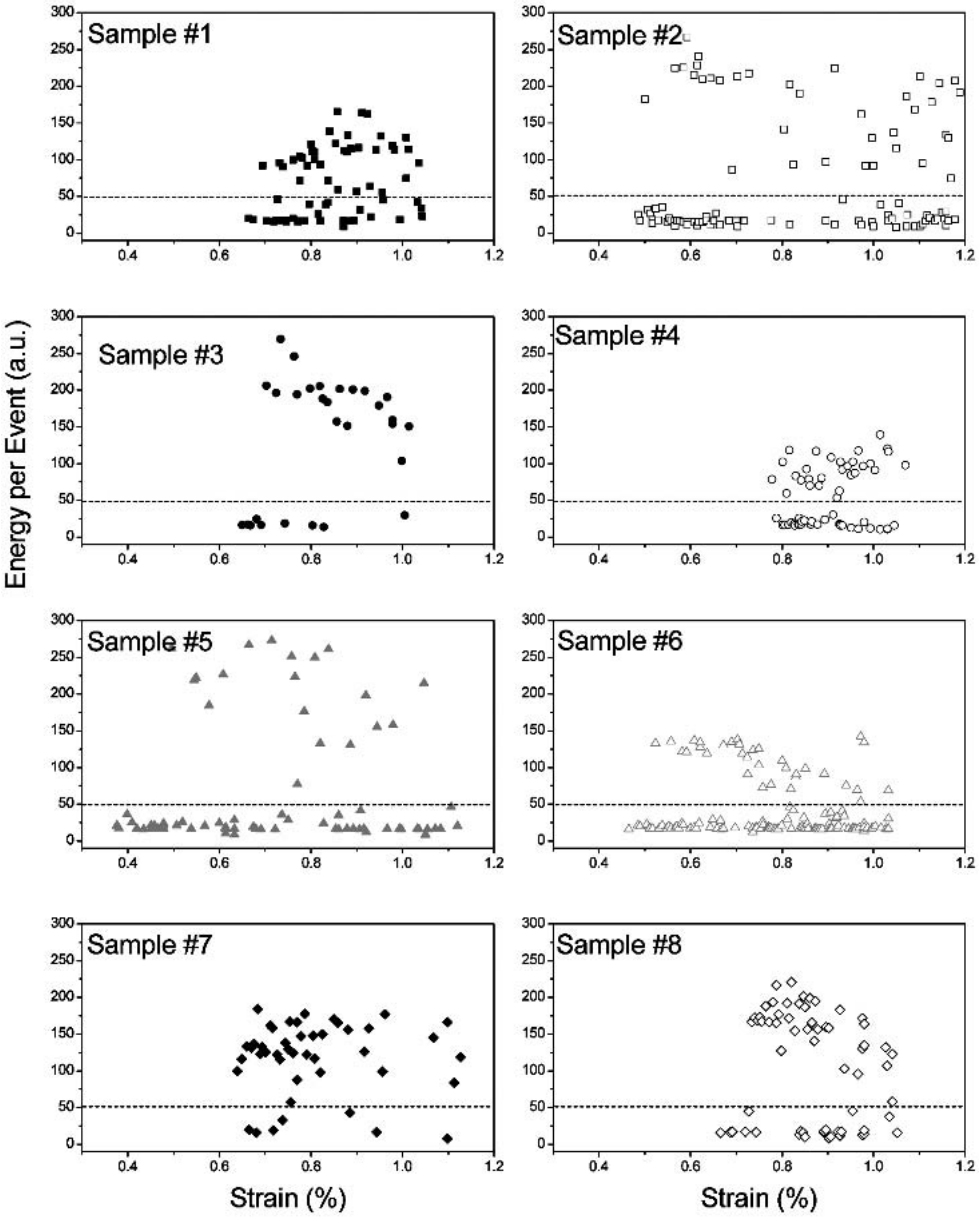

Fig. 7 AE energy of events versus strain

catastrophic failure or microcracking. As mentioned earlier, no catastrophic failure was observed in any of the coatings. Consequently, it is assumed that microcracking was the main damage mechanism in the coating microstructure during bending. Continuous monitoring of AE events during the bend test could be a reliable indicator for determining the damage mechanism in the coatings.

The first AE event corresponds to the onset of cracking. Coatings #5, #6, and #2 had the earliest crack initiation occurrence. This means that these coatings require less strain to initiate cracking. They also exhibit, over all the bending tests, a much larger number of events than the other coatings. Figure 6(a) shows the event number plotted in function of the residual stresses in the coating. The residual stress was determined from the curvature of Almen and was found to be compressive in all coatings. Of the eight points plotted, six fall almost on a straight line, which suggests a relationship between them. It was observed earlier that the coatings for which cracking were initiated first presented the highest number of event. On this basis and regarding the linearity between event number and residual stresses, one could attempt to link, by a transitive way through the event number, the onset of cracking and residual stresses. Figure 6(b) shows the onset of cracking versus residual stresses. Unfortunately, it does not show a clear relationship between them, implying that other factors may play roles. Nevertheless, it suggests that delaying the initiation of cracking could be achieved by spraying coatings that present higher compressive residual stress values. However, caution must be made on this point and more work has to be done to verify this hypothesis.

Each coating exhibited AE events of different characteristics. The distinction between them, being a weak or strong event, is expressed by the released AE energy.[1] Figure 7 reports the energy of each event as a function of strain, recorded for coatings #1 to #8. The energy of an event is defined from the signal envelope, which implies a time integration of the signal voltage output of the sensor over its duration. It can be seen that all coatings could be visibly separated in two energy distributions as delimited by dotted lines, lower and higher than 50 a.u. (arbitrary unit), a value chosen arbitrary. This distribution threshold's value could also be taken within the range of 40-60 a.u. Dalmas et al.[9] have also observed, for coatings made from WC-Co, two different types of acoustic events in term of energy. On the basis of microscopic observations, they attributed low absolute energy to transversal macrocracks and high energy to delamination. In our study, we do not have any proof that contradicts such attributions. On the contrary, these distributions illustrate clearly that weak and strong events alternate during all the range of applied strain, which corroborates the energy attribution made by Dalmas. One can also add that strong events are not generated only when approaching final failure, as showed by Lin et al.[1,13] for plasma sprayed TBCs. This confirms the damage mechanism by microcracking.

Although a coating can develop a large number of very small cracks, they could be not dangerous to its integrity. On the other hand, it can develop a few large cracks that could be deleterious for the coating structure. Therefore, the analysis of the extent of damage is better described with the AE cumulative energy. Figure 8 is a graph showing the AE cumulative energy versus strain for the deformed coatings. The cumulative energy is defined as the sum of energy of all events. This time, coatings #2, #8, #6, and #7 present higher cumulative energy values than the rest of the coatings. They also present higher cumulative energy for strong events (as shown in Table 4). It seems clear that the total cumulative energy is driven by the cumulative energy of strong events, rather than weak events.

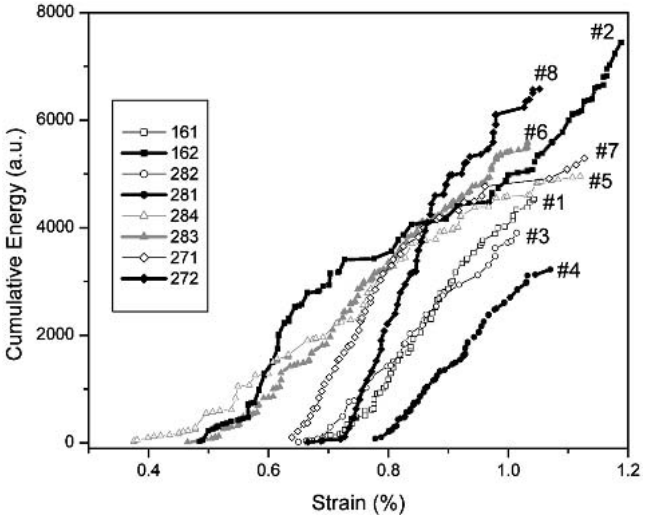

Fig. 8 AE cumulative energy versus strain

3.5 Correlations Between Microstructure and AE Features

Since none of the eight coatings spalled from the substrate, the differentiation between coatings will be made in terms of acoustic emission features, confirmed by damage extent from microstructures. Nevertheless, damage sustained by a coating has to be defined since it is application dependent. In coating applications for wear resistance purposes like corrosion or sealant, it is of primary importance to avoid the presence of cracks that could expose the substrate, otherwise coatings do not provide their intended corrosion or leak-barrier protection. With its ability to detect the occurrence of microcracking, the onset of cracking detected by acoustic emission could answer this issue. Earlier, the onset of cracking was linked to residual stresses. Thus, to maximize the coating resistance to crack initiation, one has to choose thermal spray parameter set that gives coatings high compressive residual stresses.

If one would expect to estimate the remaining lifetime of a coating before spalling or delamination or to determine the amount of damage accumulation, further investigations would have to be conducted to understand different correlations.

The examination of specimen surface during interrupted tests (low applied strain, not shown here) revealed that cracks initiated from the surface and then propagated towards the substrate. This is consistent with the fact that tensile stresses would be greatest near the coating surface. Also, it seems that all cracks are not formed simultaneously; rather, they are formed one after another. Indeed, it was observed in many coatings for which deformation was interrupted that a first crack had already propagated toward the substrate and along the interface, followed by another crack, which had also initiated from the surface and only propagated for a portion of the coating's thickness. This clearly

Table 4 AE Features for All Bent Coatings

Sample ID	Onset of Cracking, ε	Event Number	Mean Energy per Event, a.u.(a)	Cumulative Energy, a.u.(a)	Event Number, <50 a.u.(a)	Mean Energy per Event, <50 a.u(a)	Cumulative Energy, <50 a.u.(a)	Event Number, >50 a.u.(a)	Mean Energy per Event, >50 a.u.(a)	Cumulative Energy, >50 a.u.(a)
#1	0.664	67	67	4533	30	24	710	37	103	3822
#2	0.485	106	70	7446	69	18	1259	37	167	6186
#3	0.65	30	130	3905	9	19	169	21	178	3736
#4	0.778	60	53	3223	30	18	528	30	90	2695
#5	0.376	75	66	4961	55	20	1079	20	194	3881
#6	0.465	135	41	5595	101	20	2021	33	108	3573
#7	0.639	46	115	5292	7	22	155	39	132	5137
#8	0.666	63	104	6581	24	19	447	39	157	6134

(a) Abbreviation: a.u., arbitrary unit

Table 5 Effect of Spraying Parameters on AE Features

Property	Ratio H_2/O_2	Total Gas	Spray Distance	Carrier Gas	Surface Temperature	Thickness Per Pass	Interaction
Onset of cracking	−0.29	−0.83	0.15	−0.06	0.35	0.34	0.51
Total cumulative energy	−830	883	1542	−1038	−77	−735	−1062
Mean energy per event	−1.32	−39.47	16.48	27.28	9.64	−16.22	−23.29
Cumulative energy of strong events	−567	−64	1840	−502	−163	−524	−1179
Mean energy of strong event	−14	3	−2	22	−10	−11	−65
Number of events	−1.25	−0.25	11.75	−5.75	1.25	−0.75	5.25
Index of cristallinity: Ic	−0.00025	0.0567	0.0812	−0.0487	0.0187	−0.0082	0.0222
Distances between cracks	0.09	−0.13	−0.16	0.05	−0.05	0.01	−0.1
Almen N deflection	119	−50	129	0	−94	−14	−46

indicates both the progressive formation of the cracks and their distribution along the sample length.

Detailed examinations of the crack shape are shown in Fig. 3, in which the largest crack openings were observed for coatings #5, #6, #2, and #3, and the smallest for #7, #1, and #4. Note that the large crack openings seem to correlate with highest mean energy per event for strong events (> 50 a.u.), as reported in Table 4. This is in conformity with results published by Brown et al.,[14] who also observed that large cracks produced high-energy AE events. The crack opening is believed to become larger with increasing applied strain.[15]

In addition, crack spacing was found to correlate with the total cumulative energy. Indeed, with the exception of coating #1, Fig. 9(a) shows almost linearity between these two parameters. Coatings exhibiting larger crack spacing present the lower total AE cumulative energy. According to Zhou et al.,[11] the interface fracture toughness is proportional to the square root of the crack spacing, which is in our case the mean distance *d* separating two successive cracks. Thus, it is possible to establish a ranking among coatings regarding their interface fracture toughness, and on this basis, coatings #3, #4 and #5 are the toughest among the eight deformed coatings. They have, respectively, 0.99, 0.90, and 0.83 mm as separating distance *d*. Those coatings also present lower AE cumulative energy values (Table 4). Thus, associating this AE feature to coating with higher interface fracture toughness can also be done.

In another approach, as it was pointed out earlier, the WC phase, that constitutes the major phase of all coatings, has undergone a decarburization during the thermal spray process. Dependent on the thermal spray parameter set used, the carbide's degradation generated different amounts of amorphous phase. Figure 9(b) reports the total cumulative energy versus the index of crystallinity and illustrates dependence between the amount of amorphous material and the cumulative energy. The amorphous compound is suspected to be much softer than crystalline phases WC, W, and W_2C. Subsequently, coatings that have the largest amount of amorphous material are the toughest ones. Moreover, Fig. 9(c) illustrates, in a transitive manner, the linear relationship between crack spacing and phase degradation from the I_C value.

In this study, no clear correlation between microhardness and AE features was found. However, it can be said, as already reported by Cox,[7] "for applications where the toughness of a coating is of primary importance, hardness is probably not a reliable measure, but it is still valid as a quality control tool."

3.6 Choice of Thermal Spray Parameter Set Based on AE Features

From the above analysis, it seems that toughness is the key-characteristic to preserve coatings from failure by spalling or delamination. By going back to thermal spray parameter sets, we will determine which parameters influence the coatings toughness. Table 5 shows the effect of the chosen parameters on the AE features, as listed from the L-8 matrix conditions in Table 1. It can be summarized as follows:

- The spray distance influences the total cumulative energy and their event number, the AE cumulative energy of strong events, the index of crystallinity, the distance between cracks and the residual stresses.
- The total gas has an influence on the onset of cracking, the mean energy per event, as well as the index of crystallinity.
- Surprisingly, the substrate temperature has no major effect.

Thus, mainly two parameters, the total gas and spray distance are affecting the AE features and the microstructure. The choice

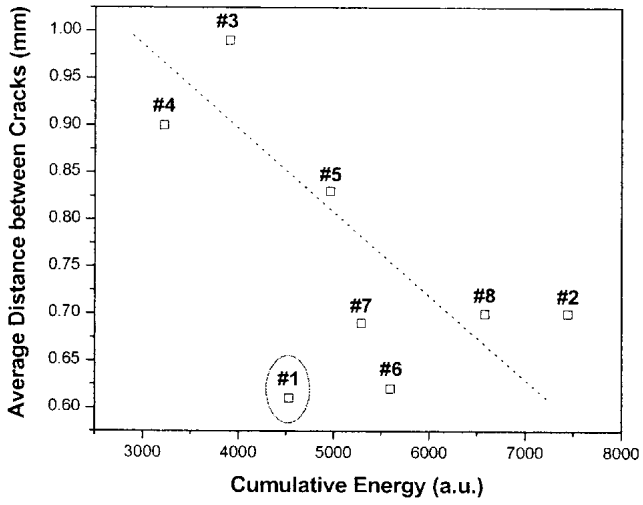

(a)

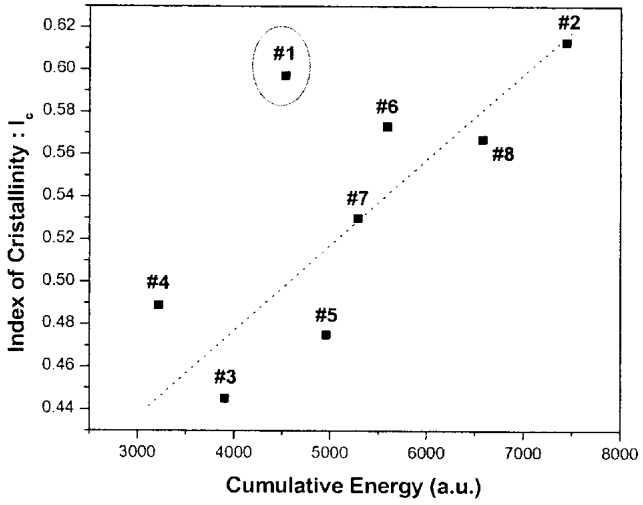

(b)

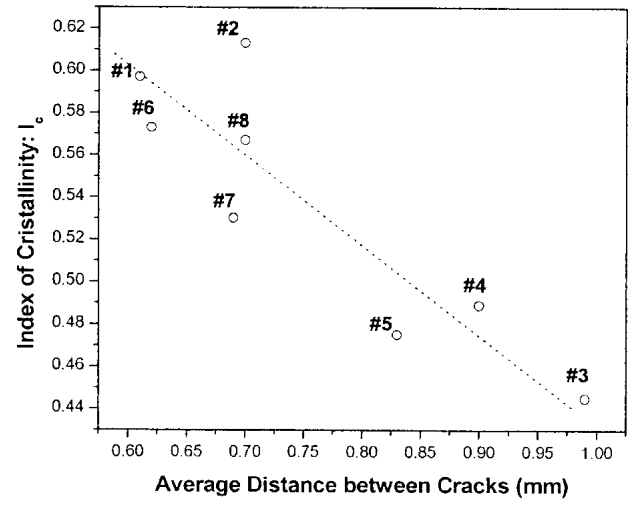

(c)

Fig. 9 **(a)** Relationship between AE cumulative energy and average distance, **(b)** relationship between cracks, **(c)** and index of crystallinity.

of the favorable thermal spray parameter set will be only based on how they influence favorably toughness through low AE cumulative energy.

3.7 Toughness Versus Spray Distance and Total Gas

As previously established, low AE cumulative energy is the signature of coatings with high toughness. Thus, on the ranking basis between coatings of low total cumulative energy and cumulative energy of strong events, as presented in Table 4, spraying at a SOD of 29.2 cm is more suitable than at 22.9 cm. The four coating sets sprayed at 29.2 cm (#3, #4, #5, and #6; Table 1) globally presented lower cumulative energy than the four coating sets sprayed at 22.9 cm (#1, #2, #7, and #8). This is in conformity to the work of Kucuk et al.,[4] where they reported that plasma sprayed coatings at shorter stand-off distance exhibited higher cracking activities. The stand-off distance condition implies that particles should have a long residence time in the flame. Moreover, among the first set of coatings, coating #3 and #4 presented the lowest AE cumulative energy. As these two coatings used the highest level of total gas (i.e., 1320 l/min), it can be stated that (toughness wise) 1320 l/min of total gas is better than 1220 l/min.

Considering the chosen stand-off distances and total gas, and looking at the average particle in-flight temperature and velocity during spraying, higher total gas produces higher temperatures and velocities independent of both stand-off distances (Fig. 2). Microstructures showed that at higher total gas, coatings underwent more carbide degradation. This could be interpreted by the fact that the increase in velocity does not sufficiently reduce the dwell time to overcome the effect of the temperature.

4. Conclusions

For all coatings, no delamination or spalling has occurred. Instead, a network of regularly spaced parallel cracks was observed on the surface of the coating and propagated through the coating toward the substrate and along the interface. Also, no catastrophic failure occurred, instead, microcracking was found to be the leading mechanism.

This study showed the ability of AE to differentiate among coatings sprayed under different thermal spray conditions. Detailed investigations showed that coatings with higher compressive residual stresses seem to have a higher resistance to crack initiation. This point has to be confirmed by adequately measuring the residual stresses with more reliable methods than the curvature of the Almen strip, like the x-ray analysis or the removal layer method.

From the damage extent observed and measured from the microstructure, the AE event number and total cumulative energy are parameters describing with enough reliability the coating's cracking activity. In particular, the distance separating cracks seems to apparently indicate the level of toughness in coatings. Also, it seems that the presence of more amorphous fraction in a coating plays a role in enhancing the toughness.

Acknowledgments

Thanks to Jan Wigren from Volvo for exchanging information regarding the bend test. Thanks to B. Harvey for software

programming, to F. Belval for HVOF spraying, to M. Lamontagne for DPV-2000 measurements, to Eric Poirier for metallography and M. Thibodeau for SEM images. The authors would like to acknowledge the participants in HCAT and C-HCAT programs for the fruitful interactions that led to the development of this work.

Appendix 1

At the center the deflection is maximal[16] and is given by:

$$\Delta_c = \frac{W_a}{24\,E\,I}(3l^2 - 4a^2) \quad \text{(Eq 1)}$$

On the other hand, strain is defined as:

$$\varepsilon = \frac{\sigma}{E} \quad \text{(Eq 2)}$$

At each load, the stress in the extreme fiber of the sample is given by:

$$\sigma = \frac{W_a}{Z} \quad \text{(Eq 3)}$$

where,

$$Z = \frac{I}{(T/2)} = \frac{2\,I}{T} \quad \text{(Eq 4)}$$

with Z the section modulus of the cross-section of the sample and I the moment of inertia of the cross-section of the sample. By substituting Eq 4 and Eq 3:

$$\sigma = \frac{W_a\,T}{2\,I} \quad \text{(Eq 5)}$$

and Eq 5 in Eq 2:

$$\varepsilon = \frac{W_a\,T}{2\,I}\frac{1}{E} \quad \text{(Eq 6)}$$

By combining Eq 6 and 5,

$$E = \frac{W_a\,T}{2\,I\,\varepsilon} \quad \text{(Eq 7)}$$

Finally, by substitution of Eq 7 into Eq 1:

$$\Delta_c = \frac{W_a}{24\,I}(3l^2 - 4a^2)\frac{2\,I\,\varepsilon}{W_a\,T} = \frac{\varepsilon}{12\,T}(3l^2 - 4a^2)$$

$$\rightarrow \varepsilon = \frac{12\,T\,\Delta_c}{(2l^2 - 4a^2)}$$

which gives strain in the extreme fiber of the sample as a function of the deflection at the center, thickness of the sample, and distances between the loading and supporting bars of the four-point bend test.

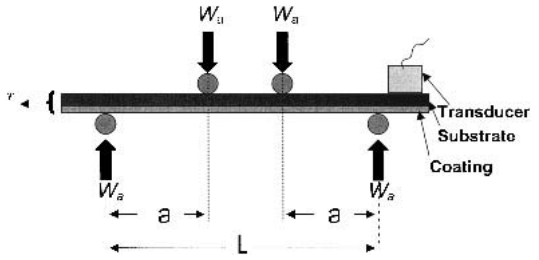

Fig. A1 Schematic illustration of the four-point bend test; W_a is the load applied at the four points; T is the thickness of the sample (substrate plus coating);. l is the distance between the two supporting bars (outer spans) of the four-point bend test; and a is the distance between adjacent loading and support bars of the four-point bend test.

References

1. C.-K. Lin, C.C. Berndt, S.-H. Leigh, and K. Murakami: "Acoustic Emission Studies of Alumina-13% Titania Free-Standing Forms During Four-Point Tests," *J. Am. Ceram. Soc.,* 1997, *80*(9), pp. 2382-94.
2. J. Voyer, F. Gitzhofer, and M.I. Boulos: "Study of the Performance of TBC Under Thermal Cycling Conditions Using an Acoustic Emission Rig," *J. Therm. Spray Technol.,* 1998, *7(2),* pp. 181-90.
3. A. Kucuk, C.C. Berndt, U. Senturk, R.S. Lima, and C.R.C. Lima: "Influence of Plasma Spray Parameters on Mechanical Properties of Yttria Stabilized Zirconia Coatings. I: Four Point Bend Test," *Mater. Sci. Eng.,* 2000, *A284,* pp. 29-40.
4. A. Kucuk, C.C. Berndt, U. Senturk, and R.S. Lima: "Influence of Plasma Spray Parameters on Mechanical Properties of Yttria Stabilized Zirconia Coatings. II: Acoustic Emission Response," *Mater. Sci. Eng.,* 2000, *A284,* pp. 41-50.
5. P. Robin, F. Gitzhofer, and M.I. Boulos: "Acoustic Emission Techniques for Life Prediction of TBCs under Thermal Cycling Conditions" in *Thermal Spray 2001: New Surfaces for a New Millenium,* C.C. Berndt, K.A. Khor, and E. Lugscheider, ed., ASM International, Materials Park, OH, 28-30 May 2001, pp. 1247-53.
6. A. Kucuk, C.G. Dambra, and C.C. Berndt: "Influence of Plasma Spray Parameters on the Cracking Behavior of Yttria Stabilized Zirconia Coatings," *Practical Failure Analysi,* 2001, *1*(1), pp. 55-64.
7. L.C. Cox: "The Four-Point Bend Test as a Tool for Coating Characterization," *Surf. Coat. Technol.,* 1988, *36,* pp. 807-15.
8. C.S. Richard, G. Béranger, J. Lu, J-F. Flavenot, and T. Grégoire: "Four-Point Bending Tests of Thermally Produced WC-Co Coatings," *Surf. Coat. Technol.,* 1996, *78,* pp. 284-94.
9. D. Dalmas, S. Benmedakhene, C. Richard, and A. Laksimi: "Characterization of Cracking Within WC-Co Coated Materials by an Acoustic Emission Method During Four Point Bending Tests" in *Proceedings of ITSC,* Montréal, Quebec, C.C. Berndt, ed., ASM International, Materials Park, OH, 2000, pp.1335-40.
10. J-G. Legoux and S. Bouaricha: "Evaluation of Starting Material and Process Parameters for HVOF WC-10Co-4Cr Coatings" in *Proceeding of ITSC,* Essen, Germany, E. Lugscheider, ed., DVS Deutscher Verbaud für Schweissen, Germany, 2002, pp. 289-94.
11. Y.C. Zhou, T. Tonomori, A. Yoshida, L. Liu, G. Bignall, and T. Hashida: "Fracture Characteristics of Thermal Barrier Coatings After Tensile and Bending Tests," *Surf. Coat. Technol.,* 2002, *157,* pp. 118-27.
12. C. Verdon, A. Karimi, and J.-L. Martin: "A Study of High Velocity Oxy-Fuel Thermally Sprayed Tungsten Carbide Based Coatings. Part 1: Microstructures," *Mater. Sci. Eng.,* 1998, *A246,* pp. 11-24.
13. C-K. Lin and C.C. Berndt: "Acoustic Emission Studies on Thermal Spray Materials," *Surf. Coat. Technol.,* 1998, *102,* pp. 1-7.
14. S.R. Brown and I.G. Turner: "Acoustic Emission Analysis of Thermal Sprayed Hydroxyapatite Coatings Examined Under Four-Point Bend Loading," *Surf. Eng.,* 1998, *14*(4), pp. 309-13.
15. K. Akita, G. Zhang, S. Takahashi, H. Misawa, and S. Tobe: "In-Situ Observation and AE Analysis of Microscopic Fracture Process of Thermal Spray Coatings" in *Proceeding of ITSC,* Nice, France, Christian Coddet, ed., ASM International, Materials Park, OH, 1998, pp. 837-42.
16. E. Oberg, F.D. Jones, H.L. Horton, and H.H. Ryffel: "Strength of Materials," *Machinery's Handbook,* R.E. Green, ed., 24th ed., Industrial Press, New York, 1992, pp. 221-22.